ADVANCED FUNCTIONAL MATERIALS
www.afm-journal.de

Polarization Sensitive Solar-Blind Ultraviolet Photodetectors Based on Ultrawide Bandgap KNb_3O_8 Nanobelt with Fringe-Like Atomic Lattice

Yue Ping, Haoran Long, Hui Liu, Chao Chen, Nannan Zhang, Hongmei Jing, Jiangbo Lu, Yiwei Zhao, Zimeng Yang, Wei Li, Fei Ma, Xiaosheng Fang, Zhongming Wei,* and Hua Xu**

Low-dimensional ultrawide bandgap semiconductors demonstrate great potential in fabricating solar-blind ultraviolet photodetectors. However, the widespread use of detectors is still limited by the low responsivity, large noise, and dark current, and especially few detectors can fulfill the solar-blind ultraviolet detection and the polarization dependence simultaneously. Herein, a polarization sensitive solar-blind ultraviolet photodetector based on ultrathin KNb_3O_8 nanobelts synthesized via chemical vapor deposition growth, is reported. By selecting suitable substrate and tuning the growth temperature, the nonlayered KNb_3O_8 crystal is grown into the quasi-1D ultrathin nanobelt with thickness in the range of 4.8–120 nm. Density functional theory calculations and experimental results indicate that the ultrathin KNb_3O_8 nanobelt possesses an ultrawide bandgap (4.15 eV) as well as unusual in-plane structural anisotropy. Benefiting from the above features, the ultrathin KNb_3O_8 nanobelt-based device exhibits superior photodetection performances with high responsivity (30 A W^{-1}), high detectivity (5.95×10^{11} Jones), and ultralow dark current (7.1×10^{-15} A) in the solar-blind ultraviolet region (230–280 nm). In addition, the KNb_3O_8 photodetector displays strong polarization sensitive photoresponse with a linear dichroic ratio of 1.62 at 254 nm. With these remarkable features, the ultrathin KNb_3O_8 nanobelt provides great opportunities for designing the next-generation multifunctional solar-blind ultraviolet optoelectronic devices.

1. Introduction

Solar-blind ultraviolet (solar-blind UV, 200–290 nm) photodetectors based on ultrawide bandgap semiconductors (UWBSs) have extremely important applications in optical communications, chemical/biological analysis, environment monitoring, and optoelectronic devices.[1–4] Previously, the state-of-the-art solar-blind UV photodetectors based on UWBSs, such as SiC, diamond,[5] II-oxides,[6] and III-nitride materials,[7] serving as high-performance active layers have been widely reported. To meet the requirements of next-generation high-performance photodetectors, including energy-efficient, miniaturization, flexibility, and multifunction applications,[8–9] exploring novel active layers has become an important objective. Low-dimensional materials are considered promising candidates to address the above challenges owing to their rich structures, tunable bandgap, high carrier mobility, strong light-matter interactions, and good compatibility with silicon-based semiconductor technology.[10–14] Taking the widely

Y. Ping, C. Chen, N. Zhang, Z. Yang, W. Li, H. Xu
Key Laboratory of Applied Surface and Colloid Chemistry
Ministry of Education
Shaanxi Key Laboratory for Advanced Energy Devices
School of Materials Science and Engineering
Shaanxi Normal University
Xi'an 710119, P. R. China
E-mail: xuhua-nano@snnu.edu.cn

H. Long, Z. Wei
State Key Laboratory of Superlattices and Microstructures, Institute of Semiconductors
Chinese Academy of Sciences & Center of Materials Science and Optoelectronics Engineering
University of Chinese Academy of Sciences
Beijing 100083, P. R. China
E-mail: zmwei@semi.ac.cn

H. Liu, X. Fang
Department of Materials Science
Fudan University
Shanghai 200433, P. R. China
E-mail: xshfang@fudan.edu.cn

H. Jing, J. Lu
School of Physics and Information Technology
Shaanxi Normal University
Xi'an 710119, P. R. China

Y. Zhao, F. Ma
State Key Laboratory for Mechanical Behavior of Materials
School of Materials Science and Engineering
Xi'an Jiaotong University
Xi'an 710049, P. R. China

The ORCID identification number(s) for the author(s) of this article can be found under https://doi.org/10.1002/adfm.202111673.

DOI: 10.1002/adfm.202111673

studied 2D materials as examples, such materials cover a vast range of bandgaps from the terahertz in bilayer graphene, the NIR and visible in numerous transition metal dichalcogenides to the ultraviolet in h-BN.[15–18] However, most 2D semiconductors are not competent for solar-blind UV detection due to their relatively small bandgap (<2.5 eV).[15] Although several 2D wide bandgap (up to 3.40 eV) semiconductors can be used to detect UV light,[19–21] the low detection capability and the poor wavelength selectivity in solar-blind UV photodetection hinder their practical applications.

Another significant issue that comes with the extending research on low-dimensional material-based photodetectors is related to the polarization sensitive detection, which induces a novel physical degree of freedom for modulating the optoelectronic detection and thus provides the possibility for improving the detection accuracy and intelligence.[22–25] The polarization sensitive photodetectors based on various anisotropic low-dimensional materials (such as black phosphorus, $GeSe_2$, ReS_2, $PdSe_2$, Bi_2S_3, $GeAs_2$, etc.) are primarily response to the visible light.[24–33] However, due to the lack of low-dimensional UWBSs with intrinsic structural anisotropy, the polarization sensitive photodetection in solar-blind UV region still remain scarce. Hence, it is highly desired to explore new kinds of low-dimensional UWBSs with intrinsic in-plane structural anisotropy and excellent optoelectronic properties.

Low-dimensional ternary transition metal oxides have recently attracted increasing research interests due to their diverse structures and superior properties including exciton insulating phase, intrinsic ferromagnetism, and ultrahigh carrier mobility.[34–36] Among them, ternary KNb_3O_8 is predicted to possess the wide bandgap, superior dielectric properties as well as the possible structural anisotropy,[37–38] which endows it a promising material for the polarization sensitive solar-blind UV photodetector. In the past reports, low-dimensional KNb_3O_8 materials synthesized via sol-gel or hydrothermal methods were widely applied in photocatalysis and lithium ion battery.[39–43] However, the disordered morphology of thick KNb_3O_8 nanoflakes synthesized by the above methods cannot be used in micro-nano devices due to incompatibility with semiconductor processing technology. The low crystallinity, numerous oxygen defects, and unavoidable surface contamination of the liquid-phase synthesized KNb_3O_8 nanoflakes also hinder its development in optoelectronic devices. Therefore, to date, fabrication of KNb_3O_8 nanostructures with high crystallinity has never been reported for polarization sensitive solar-blind UV detection devices.

In this work, we report the synthesis of large-scale ultrathin KNb_3O_8 nanobelts via chemical vapor deposition (CVD) growth and the exploration of its solar-blind UV photodetection applications. By selecting suitable substrate and tuning the growth temperature, the nonlayered KNb_3O_8 crystal was grown into the quasi-1D ultrathin nanobelt. Structure characterizations confirm the orthorhombic phase structure of KNb_3O_8 nanobelt with high crystallinity. Density functional theory (DFT) calculations combined with optical characterizations demonstrate that the ultrathin KNb_3O_8 nanobelt possesses an ultrawide bandgap (4.15 eV), a broadband photoluminescence (PL) emission and an intrinsic in-plane structural anisotropy. As results, the KNb_3O_8 nanobelt-based device displays excellent photoresponse under the solar-blind UV region (254 nm) with high responsivity up to 30 A W^{-1} and strong polarization sensitivity (linear dichroic ratio of 1.62). Moreover, aging experiments demonstrate the superior air stability of the KNb_3O_8 nanobelt-based solar-blind UV photodetector.

2. Results and Discussion

KNb_3O_8 crystal possesses an orthorhombic structure (Cmcm, No. 63) with lattice constants of a = 8.903, b = 21.16, and c = 3.799 Å. As schematically shown in **Figure 1**a, KNb_3O_8 crystal consists of negatively charged sheets of linked NbO_6^- octahedral units and K^+ ions between the sheets. In this regard, it is possible to synthesis the nonlayered KNb_3O_8 crystal into the 2D nanosheet or the quasi-1D nanobelt via reasonably controlling the growth conditions. Density functional theory (DFT) calculations show that the KNb_3O_8 crystal possesses a large bandgap of 3.94 eV (Figure 1b), where the conductive band minimum (CBM) and valance band maximum (VBM) are located in the Γ point and U point, respectively. According to the partial density of state, Nb_d orbital and O_p orbital occupy the VBM, while the CBM is mainly contributed by the Nb_d orbital. Moreover, the partial charge density (PCD) was calculated to evaluate the anisotropic properties of KNb_3O_8 crystal. The spatial distribution of CBM and VBM wave functions shows obvious distinction on the *ac*-plane (Figure 1c) and *bc*-plane (Figure 1d), suggesting the intrinsic in-plane anisotropic optical property of KNb_3O_8 crystal. Such anisotropic property of KNb_3O_8 is dominantly originated from its structural anisotropy. Above theory results indicate KNb_3O_8 an ideal candidate for solar-blind UV optoelectronic applications.

The synthesis of KNb_3O_8 crystal via CVD growth is schematically shown in Figure S1 in the Supporting Information. Briefly, the mixture of Nb_2O_5 and KCl powder with mass ratio of 1:3 was loaded in a quartz boat, the freshly cleaved mica was used as the growth substrate, and they were placed at the heating center of the tube furnace. The CVD growth was performed at 800 °C with Ar as carry gas for 10 min. More details about the sample synthesis procedure are shown in the experiment section. Figure 1e shows the optical microscopy (OM) image of as-grown large-scale KNb_3O_8 on mica, where the samples exhibit a nanobelt-like quasi-1D morphology with an average length and width of ≈80 and 5 µm, respectively. The energy-dispersive spectroscopy (EDS) of the sample (Figure S2a, Supporting Information) reveals the atomic ratio of 1:3:8, confirming the stoichiometric ratio of KNb_3O_8 nanobelt. X-ray photoelectron spectroscopy (XPS) results (Figure S3, Supporting Information) indicate that the Nb in the KNb_3O_8 sample is in the Nb^{5+} state with the measured binding energy ($3d_{5/2}$, ≈206.3 eV) located between Nb^{6+} in NbO_3 ($3d_{5/2}$, ≈207.2 eV) and Nb^{4+} in NbO_2 ($3d_{5/2}$, ≈205.9 eV). X-ray radiation diffraction (XRD) spectrum (Figure S2b, Supporting Information) is consistent with the standard diffraction patterns of KNb_3O_8 crystal (PDF#75-2182), suggesting the orthorhombic phase structure and the high crystal quality. Atomic force microscope (AFM) image of the KNb_3O_8 nanobelt (inset in Figure 1e) shows a smooth surface with a thickness of about 9.0 nm. Note that the nanobelt shape of CVD-grown KNb_3O_8 is distinctively different from the

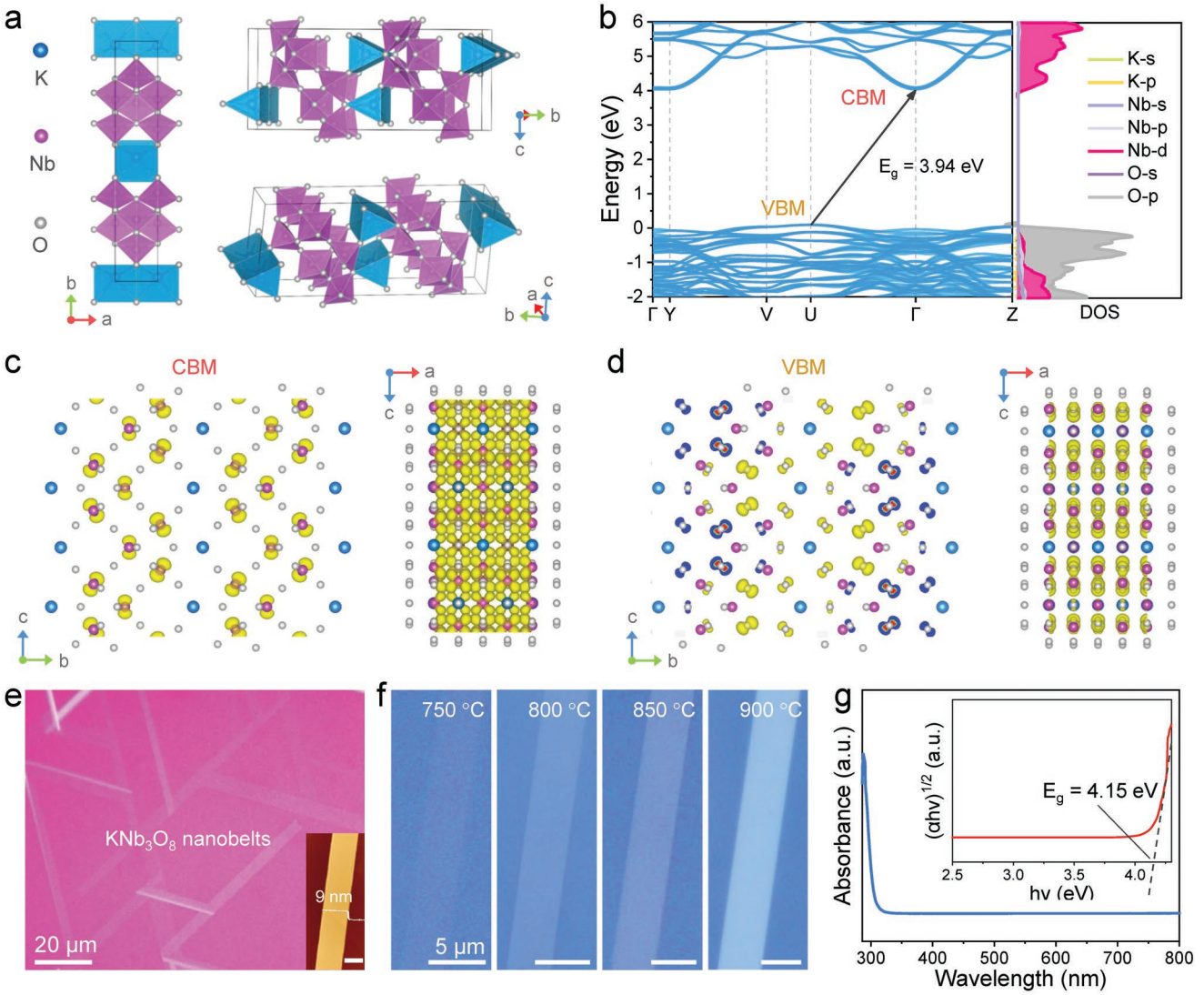

Figure 1. Crystalline structure, electronic band structure, and synthesis of KNb_3O_8 crystal. a) Atomic structure of KNb_3O_8 crystal with different lattice faces, the blue, purple, and gray sphere represent K, Nb, and O atom, respectively. b) DFT band structure for a 7×7 supercell of KNb_3O_8 crystal. Also shown is the projected density of states (DOS) of Nb_d in pink shades and the O_p in gray shades. c,d) Partial charge density of CBM and VBM, respectively. e) Typical OM image of CVD-grown large-scale ultrathin KNb_3O_8 nanobelts on mica substrate. Inset is the corresponding AFM image of one KNb_3O_8 nanobelt. f) OM images of representative KNb_3O_8 nanobelt grown at 750, 800, 850, and 900 °C on mica substrate. g) UV–vis absorption spectrum of CVD-grown KNb_3O_8 nanobelts. Inset is the corresponding Tauc curve.

cylinder shape KNb_3O_8 nanorod synthesized by traditional liquid-phase synthesis methods.[39] It was found that the ultrathin KNb_3O_8 nanobelts can only be grown on mica substrate, while cylinder shape KNb_3O_8 nanorods were obtained on sapphire substrate (Figure S4, Supporting Information). This is reasonable, because the inert and flat surface of mica has a low energy barrier for atom migration, which together with the anisotropic structure of KNb_3O_8 crystal favors its epitaxial growth into the quasi-1D nanobelts. Moreover, the KNb_3O_8 nanobelts grown on mica substrate present three primary orientations (0°, 120°, and –120°, Figure S5, Supporting Information), which is consistent with the six-fold symmetry structure of mica.

To achieve precise control of the synthesis, we explored the growth of KNb_3O_8 crystal at temperature ranging from 700 to 900 °C (Figure S6a–e, Supporting Information). Figure 1f shows the typical OM images of KNb_3O_8 nanobelt grown at 750, 800, 850, and 900 °C, where the obvious optical contrast difference of these samples indicates the thickness variation. As the increase of growth temperature, the domain length and thickness of KNb_3O_8 nanobelts increase from 40 to 350 μm and 4.8 to 120 nm, respectively (Figures S6f and S7, Supporting Information). Furthermore, absorption spectrum (Figure 1g) of the as-grown KNb_3O_8 nanobelts shows a narrow UV wavelength region with absorption edge around 300 nm and absorption peak below ≈280 nm. Tauc curve (inset in Figure 1g) extracted from the absorption spectrum demonstrates that the optical bandgap of KNb_3O_8 nanobelt up to ≈4.15 eV which is close to the theory calculated bandgap (≈3.94 eV). The slight bandgap disparity might be attribute to the parity-forbidden transitions between valence and conduction band, since KNb_3O_8 adopts

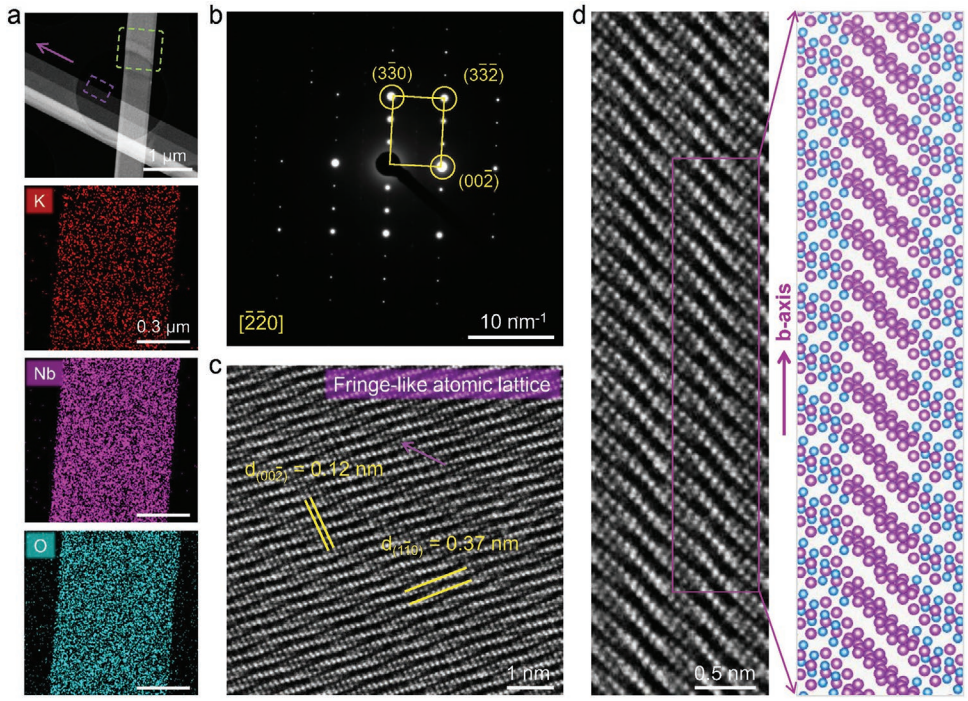

Figure 2. Composition and structure characterization of CVD-grown KNb_3O_8 nanobelts. a) Low-magnification ADF-STEM image of KNb_3O_8 nanobelts and corresponding EDS element mapping of K, Nb, and O elements. b) SAED patterns of KNb_3O_8 nanobelt. c) High-resolution ADF-STEM image of KNb_3O_8 nanobelt. d) Enlarged high-resolution ADF-STEM image of KNb_3O_8 nanobelt and the corresponding crystallographic structure model, where the O atoms are omitted for clearly distinguishing the structure.

a crystal structure (orthorhombic, space group Cmcm, No.63) possessing inversion symmetry.[44]

To examine the crystallographic structure of the CVD-grown ultrathin KNb_3O_8 nanobelts, aberration-corrected annular dark-field scanning transmission electron microscopy (ADF-STEM) was conducted on the samples. The low-magnification STEM image of KNb_3O_8 nanobelts and the corresponding EDS elemental mapping images acquired at the green-dashed area (**Figure 2**a) demonstrate the homogeneous spatial distribution of K, Nb, and O elements throughout the entire sample. Selected-area electron diffraction (SAED) pattern of the sample reveals a single set of electron diffraction spots (Figure 2b), indicating the single crystal feature of orthorhombic structured KNb_3O_8 nanobelt. Figure 2c shows the high-resolution ADF-STEM image of KNb_3O_8 crystal, where the bright and dim sites are corresponding to the Nb (Z = 41) and K (Z = 19) atoms, respectively. Note that the O atom (Z = 8) is difficult to be observed in the STEM image due to its much smaller atomic number. We can see a nearly perfect periodic atom arrangement with the clearly resolved lattices spacing of 0.12 and 0.37 nm which are corresponding to the (00-2) and (1-10) planes of the KNb_3O_8 crystal. The uniform Z contrast and nearly absence of local discontinuity or topological defect in the STEM image indicate the high crystallinity of CVD-grown KNb_3O_8 nanobelts. Notably, a fringe-like atom arrangement along the long-axis direction of the KNb_3O_8 nanobelt can be clearly resolved from the STEM image (Figure 2c; Figure S8, Supporting Information), indicating a prominent in-plane structural anisotropy. The enlarged STEM image of KNb_3O_8 nanobelt and the corresponding crystallographic structure (Figure 2d) further confirm its intrinsic in-plane structural anisotropy, where the distinctive spiral-like structure misstacked by the periodic NbO_6 atomic cluster forms the fringe-like atom arrangements. Accordingly, the other two side views of the KNb_3O_8 nanobelt (Figure S9, Supporting Information) can also reveal its in-plane structural anisotropy.

Raman spectrum was measured to assess the phonon band and structure information of the ultrathin KNb_3O_8 nanobelts. It was found that the KNb_3O_8 nanobelt owns rich Raman active modes at 155, 178, 216, 248, 321, 352, 450, 893, and 950 cm^{-1} (Figure S10, Supporting Information). In the high frequency zone, the peak at 950 cm^{-1} is attributed to the stretching vibration of the short Nb—O bonds in the distorted NbO_6 unit, and the peak at 893 cm^{-1} corresponds to the NbO_6 octahedron mode.[43] In the middle frequency region, the peak at 450 cm^{-1} is attributed to the bending vibration modes of Nb—O—Nb, and the peak at 321 cm^{-1} corresponds to the deformed NbO_6 octahedral framework. The lower frequency bands in the range of 155–248 cm^{-1} are related to the Nb—O framework. As the thickness increase of KNb_3O_8 nanobelts, the peak intensity of these Raman modes gradually increase, while their peak position maintains well (Figure S6g,h, Supporting Information), which are the typical Raman features of the nonlayered crystal. Furthermore, angle-resolved polarized Raman spectroscopy (ARPRS) was conducted to reveal the anisotropic properties and crystal orientations of the ultrathin KNb_3O_8 nanobelts. As shown in **Figure 3**a, Raman mapping images at 155, 216, and 893 cm^{-1} of KNb_3O_8 nanobelts with three orientations show obvious intensity difference, suggesting an orientation-dependent Raman feature. The Raman intensity exhibits

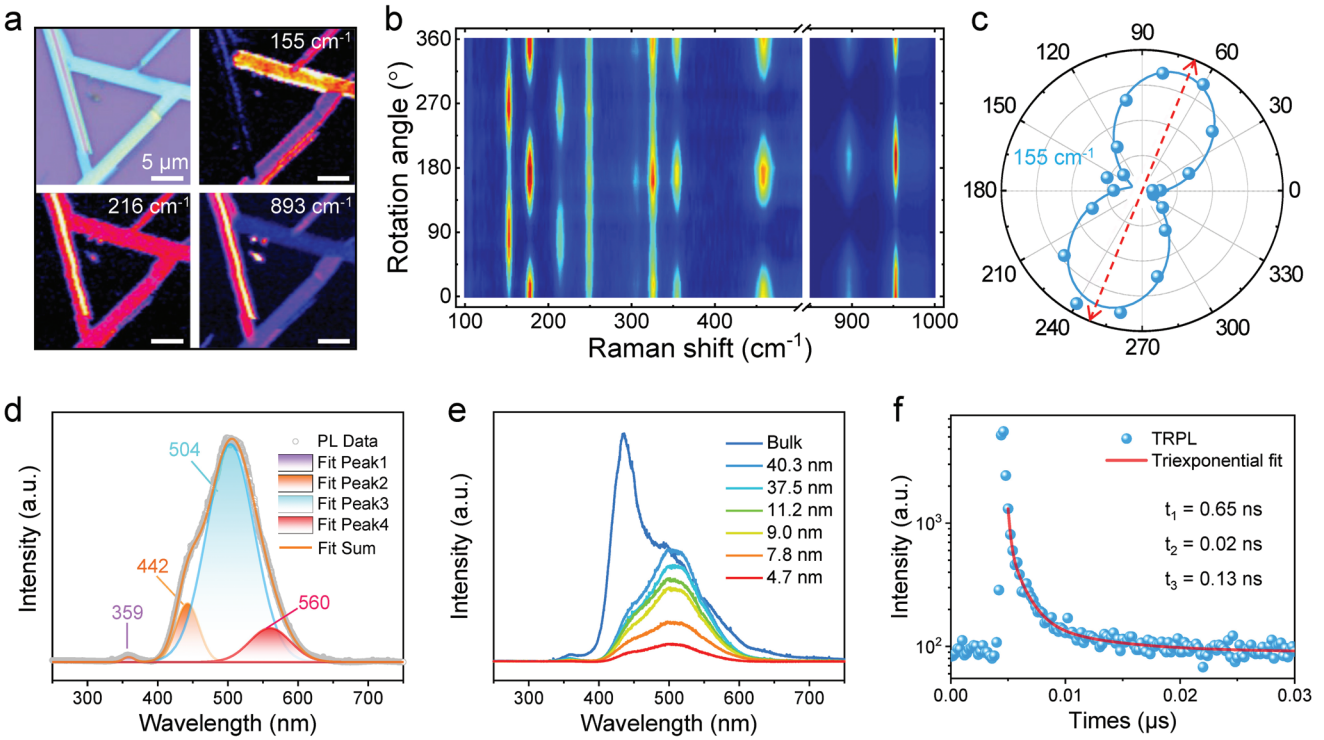

Figure 3. Optical properties of ultrathin KNb_3O_8 nanobelts. a) Raman mapping for the peak intensity of KNb_3O_8 nanobelts at 155, 216, and 893 cm^{-1}. b) 2D mapping of Raman spectra regarding to the polarization angle (θ) of the incident light. The Raman intensity was processed via normalization. c) Polar plots for the Raman peak intensity at 155 cm^{-1} with respect to θ. d) Gaussian-fitted room-temperature PL emission spectrum of a KNb_3O_8 nanobelt with thickness of ≈25 nm. e) Room-temperature PL emission spectra of KNb_3O_8 nanobelts with different thickness under a 325 nm laser excitation. f) The TRPL spectrum of ultrathin KNb_3O_8 nanobelts.

periodic variation with the polarization angle (θ) of incident light changing from 0° to 360° (Figure 3b; Figure S10a, Supporting Information), confirming the strong in-plane structural anisotropy of ultrathin KNb_3O_8 nanobelts. Note that the direction of the maximum of Raman peak intensity at 155 cm^{-1} is corresponding to the long-axis direction (the long-axis and short-axis direction are defined as *b*-axis and *a*-axis, respectively) of the KNb_3O_8 nanobelt (Figure 3c; Figure S10b, Supporting Information), which can thus be utilized to identify its lattice orientation.

Photoluminescence (PL) spectrum of KNb_3O_8 nanobelt demonstrates a broadband PL emission (340–640 nm), as shown in Figure 3d. The PL spectrum of KNb_3O_8 nanobelt can be fitted into four bands by using Gaussian fit. The main PL peak at 504 nm originates from the intrinsic NbO_6 octahedrons, while the peak at 560 nm is attributed to the extrinsic NbO_6 octahedrons, such as oxygen deficiencies.[45] The PL peaks at 359 and 442 nm are ascribed to the band-to-band recombination and the bound exciton recombination in KNb_3O_8 crystal, respectively. The PL spectra of KNb_3O_8 nanobelts with thickness ranging from tens of nanometers to sub-nanometer indicate that the absolute emission intensities gradually decrease with the reduction of thickness (Figure 3e). Note that the ultrathin KNb_3O_8 nanobelt, even for the 4.7 nm sample, still maintains steady white-light emissions, suggesting great potential in white-light source related applications. Moreover, the shape of PL spectrum shows an obvious mutation when the thickness increases to bulk, indicating a prominent quantum size effect of KNb_3O_8 crystal. Time-resolved photoluminescence (TRPL) spectrum was performed to determine the lifetime and kinetics of the photogenerated carriers in KNb_3O_8 nanobelt (Figure 3f). Three time constants extracted from the triexponential fitting curve are 6.5, 0.2, and 1.3 ns, and the average lifetime is 3.3 ns. The two shorter time constants (0.2 and 1.3 ns) show a fast PL decay process, which are related to the free carrier recombination, and another longer time constant (6.5 ns) is attributed to the formation of the binding exciton and subsequent radiation annihilation. These processes are consistent with the corresponding frequency bands in the PL emission spectrum.

The ultrawide bandgap of KNb_3O_8 nanobelt motivated us to explore its attractive application in solar-blind UV photodetection. As schematically shown in **Figure 4**a, the as-grown ultrathin KNb_3O_8 nanobelts were transferred onto a SiO_2/Si substrate (300 nm), and then the two-electrode KNb_3O_8 photodetectors were constructed via the standard device fabrication procedures. Figure 4b shows the dark-field and bright-field OM images of the KNb_3O_8 nanobelt device. As expected, the output curves (I_{ds}–V_{ds}) under dark and light illumination by varied wavelength in Figure 4c reveal that the KNb_3O_8 device shows a sensitive photoresponse from near-UV (380 nm) to solar-blind UV (260 nm) light. The photodetector yields an ultralow dark current of 7.1×10^{-15} A at 3.0 V bias voltage and a photocurrent up to 28.0 nA under 260 nm illumination. The high on/off ratio over 10^6 indicates that the KNb_3O_8 nanobelt responds effectively

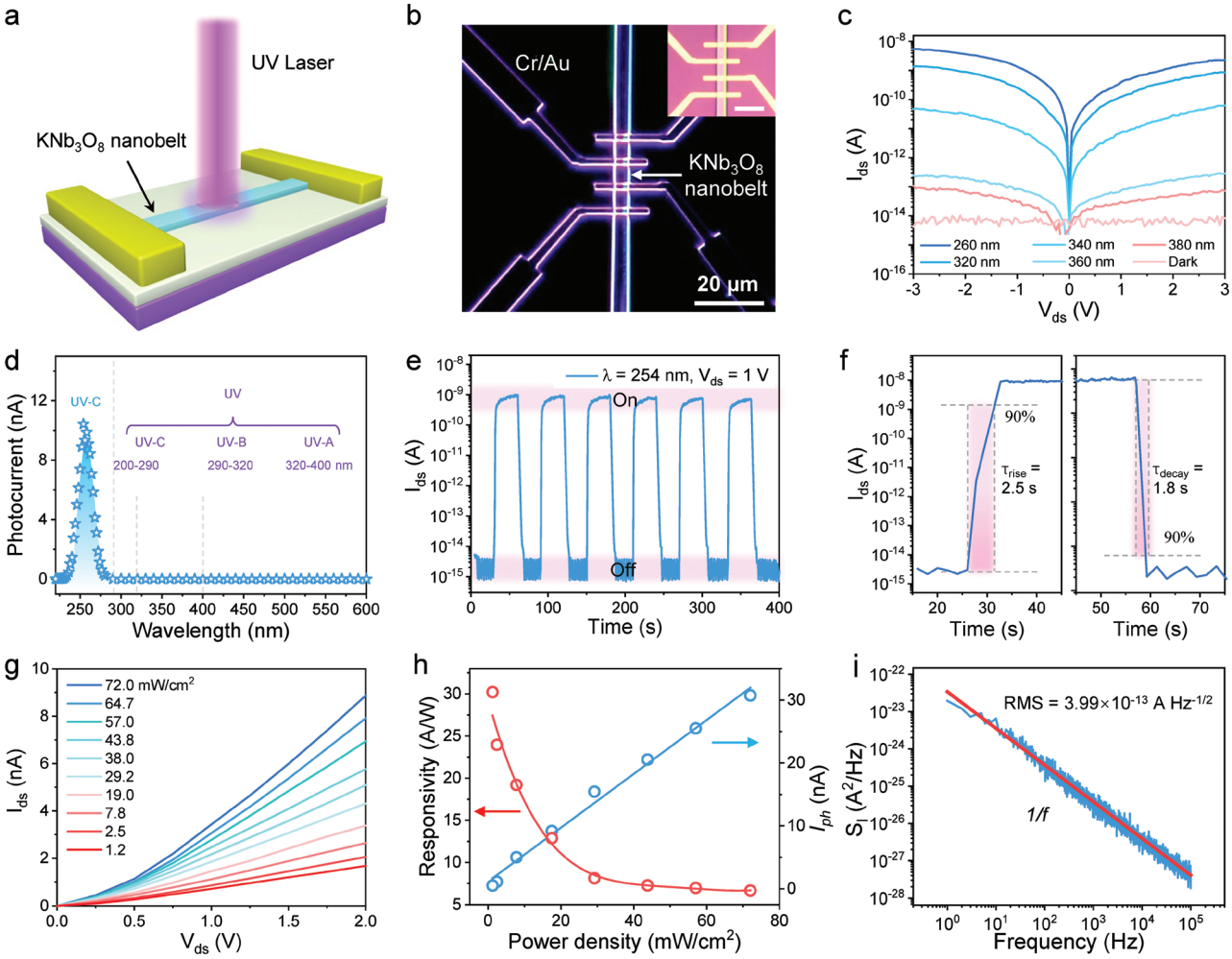

Figure 4. Photodetection based on ultrathin KNb_3O_8 nanobelt. a) Schematic diagram for the photoelectric measurement of the device. b) Dark-field OM image of the KNb_3O_8 nanobelt device. Inset is the corresponding bright-field OM image, the scale bar is 20 μm. c) I_{ds}–V_{ds} curves of the device in dark and under UV light illumination with different wavelength. d) Photocurrent as a function of wavelength ranging from 240–600 nm at V_{ds} = 3 V. The inset shows the defined wavelength range of UV-C (200–290 nm), UV-B (290–320 nm), and UV-A (320–400). e) I_{ds}–time curve under 254 nm UV on/off switching at V_{ds} = 1 V. f) Enlarged views of single on/off cycle of the device. g) I_{ds}–V_{ds} curves under dark and light illumination with different power density. h) Photocurrent and responsivity as a function of power density of light. i) Current noise power density spectrum of the ultrathin KNb_3O_8 nanobelt photodetector.

to the incident solar-blind UV light. Moreover, the wavelength-dependent photocurrent curve (Figure 4d) reveals a narrow-band photoresponse (230–280 nm) with a full-width at half-maximum of ≈22 nm, which enables KNb_3O_8 specific wavelength photodetection in the UV-C region (200–290 nm). The cutoff wavelength at ≈280 nm corresponds with the optical bandgap achieved from UV–vis absorption spectrum in Figure 1g.

The transient photoresponse (I_{ds}–time) of KNb_3O_8 photodetector measured under 254 nm light on/off switching shows high repeatability and fast response speed (Figure 4e). The rise time (τ_{rise}) and decay time (τ_{decay}) were estimated to be about 2.5 and 1.8 s (Figure 4f), which are close to those of the 2D photodetectors based on MoS_2, ReS_2, SiAs, etc.[46–48] The I_{ds}–V_{ds} (Figure 4g) and I_{ds}-time (Figure S11, Supporting Information) curves of the device under 254 nm light illumination with power density ranging from 1.2 to 72.0 mW cm^{-2} show that the photocurrent increases gradually with the increase of the light power. We describe the photocurrent (I_{ph}) as a function of the incident light intensity (P) by fitting it with equation of $I_{ph} = \alpha P^{\theta}$, as shown in Figure 4h. The fitting value θ = 0.83 shows a sublinear behavior, indicating the photocurrent is determined by a photoconductive mechanism. One can find that the responsivity is up to 30 A W^{-1} (the external quantum efficiency and detectivity are estimated to be 146% and 5.95 × 10^{11} Jones, respectively) under 254 nm light illumination (1.2 mW cm^{-2}). The responsivity of KNb_3O_8 photodetector is higher than most of the other reported 2D and 1D UV photodetectors (**Table 1**), which may be a result of the high crystal quality of KNb_3O_8 nanobelt and the strong light-matter interaction. Figure 4i shows the noise frequency characteristic (S–f) of KNb_3O_8 device under a weak light field (6 mW cm^{-2}) at 254 nm wavelength, where S is the power spectral density of noise. The photodetector exhibits a lower noise current of 4.41 pA at the frequency of 1 Hz. According to the Hooge empirical law, the curve can

Table 1. Summary of 1D and 2D photodetectors.

Material	Wavelength [nm]	Polarization sensitive	Responsivity [A W^{-1}]	Detectivity [Jones]	Dark Current [A]	Rise/decay time [ms]	Reference
$ReSe_2$	850	Yes	8.4	458	3.35×10^{-7}	5.47/8.41	[61–62]
Sb_2Se_3 nanowire	532	Yes	5	4.4×10^{9}	–	32/5	[58]
Bi_2S_3	360	Yes	0.012	–	–	–	[31]
$GeSe_2$	355	Yes	0.125	1.2×10^{15}	2.5×10^{-14}	30	[20]
SiAs	325	Yes	0.016	1×10^{10}	1.0×10^{-12}	3000/1500	[48]
MoS_2	561	No	880	–	2.0×10^{-12}	4000/9000	[46]
GaN	360	No	0.15	7.2×10^{9}	–	280/450	[63]
ZnO nanowire	355	No	0.0075	–	4.5×10^{-6}	$5 \times 10^{-7}/6.7 \times 10^{-3}$	[64]
CuBr	345	No	3.17	1.4×10^{11}	6.4×10^{-13}	48/32	[21]
$Sr_2Nb_3O_{10}$	270	No	1.21	1.4×10^{14}	2.1×10^{-12}	0.4/40	[50]
$NiPS_3$	254	No	0.126	1.22×10^{12}	10^{-14}	3.2/15.6	[57]
BiOCl	250	No	35.7	2.2×10^{10}	1.37×10^{-11}	–	[56]
h-BN	212	No	0.0001	2.4×10^{8}	10^{-11}	320/630	[18]
KNb_3O_8 nanobelt	254	Yes	30	5.95×10^{11}	7.1×10^{-15}	2500/1800	This work

be fitted by equation of $S = S_0 I^{\beta}/f^{\alpha}$, where S_0 is the Hooge parameter, I is the current through the detector, f is the frequency, and α and β are two fitting parameters. After fitting, α is equal to 0.98, which is very close to 1. Hence, the noise of KNb_3O_8 device is mainly $1/f$ noise, which usually comes from the fluctuations in the process of carrier transport. Moreover, the KNb_3O_8 photodetector exhibits superior stability under ambient air condition, with negligible photocurrent reduction after 6 months aging in air (Figure S12, Supporting Information).

Based on the intrinsic in-plane structural anisotropy of KNb_3O_8 nanobelt, we further studied the linear dichroism of this material by measuring the polarization-dependent photoresponse at the solar-blind UV region, as schematically shown in **Figure 5**a. Figure 5b shows prominent polarization-dependent photocurrent at bias voltage from 0 to 5 V under the UV light illumination of 254 nm. It can be seen that the measured photocurrent is highly dependent on the bias voltage and the polarization angle. Through switching the on-off state of the laser and simultaneously tuning the polarization angle of the light via a half-wave plate, we continuously recorded the dynamic photoresponse of the KNb_3O_8 nanobelt. As shown in Figure 5c, the photocurrent demonstrates dramatically periodic changes with the maximum and the minimum values obtained along the *b*-axis and the *a*-axis directions of KNb_3O_8 nanobelt, respectively. The extracted photocurrent plotted in Figure 5d, which was fitted by the following function $I_{ph} = I_{pha}cos^2(\phi) + I_{phb}sin^2(\phi)$, show a large anisotropic ratio ($I_{\text{ph-max}}/I_{\text{ph-min}}$) about 1.62 was achieved. The above results suggest a strong polarization sensitive solar-blind UV photodetector based on the ultrathin KNb_3O_8 nanobelt. Figure 5e summarizes the photoresponse range and the anisotropic ratio of the main 2D and 1D materials. Obviously, the photoresponse of most of these materials is located in the UV-A and UV-B regions, the ultrathin KNb_3O_8 nanobelt exhibits the optimal anisotropic optoelectronic performance at the UV-C (solar-blind UV) region. Notably, one recent progress on polarization sensitive solar-blind ultraviolet photodetector was also achieved based on 2D GaPS4,[49] but it lacks the necessary wavelength selectivity. Furthermore, one can find that the overall performance of KNb_3O_8 photodetector is superior to most of the other reported 2D and 1D UV photodetectors (Table 1), demonstrating great prospects for designing future multifunctional solar-blind UV optoelectronic devices.

3. Conclusion

In summary, large-scale ultrathin KNb_3O_8 nanobelts with high crystallinity have been successfully synthesized via CVD growth. By precisely tuning the growth temperature, the domain length and thickness of ultrathin KNb_3O_8 nanobelt can be modulated from 40 to 350 μm and 4.8 to 120 nm, respectively. Theory simulations combined with optical characterizations demonstrate that the KNb_3O_8 nanobelt possesses an ultrawide bandgap (4.15 eV) with a board band emission (340–640 nm). Furthermore, the KNb_3O_8 nanobelt-based device demonstrates outstanding photoresponse to the solar-blind UV light (254 nm), with responsivity of 30 A W^{-1}, detectivity of 5.95×10^{11} Jones and dark current of 7.1×10^{-15} A. In particular, the photodetector exhibits strong linear dichroic to the solar-blind UV light, benefiting from its intrinsic in-plane structural anisotropy. The aging experiments of KNb_3O_8 nanobelt and device in ambient air indicate its superior air stability. This work not only enriches the synthesis approach of alkaline niobates, but also sheds light on the development of high-performance and multifunctional optoelectronic devices in the solar-blind UV region based on stable low-dimensional UWBSs in the future.

4. Experimental Section

Growth and Transfer of KNb_3O_8 Nanobelts: High quality 2D KNb_3O_8 nanobelts were synthesized in a single-temperature-zone quartz tube furnace through an ambient pressure CVD technique. Niobium (V) oxide

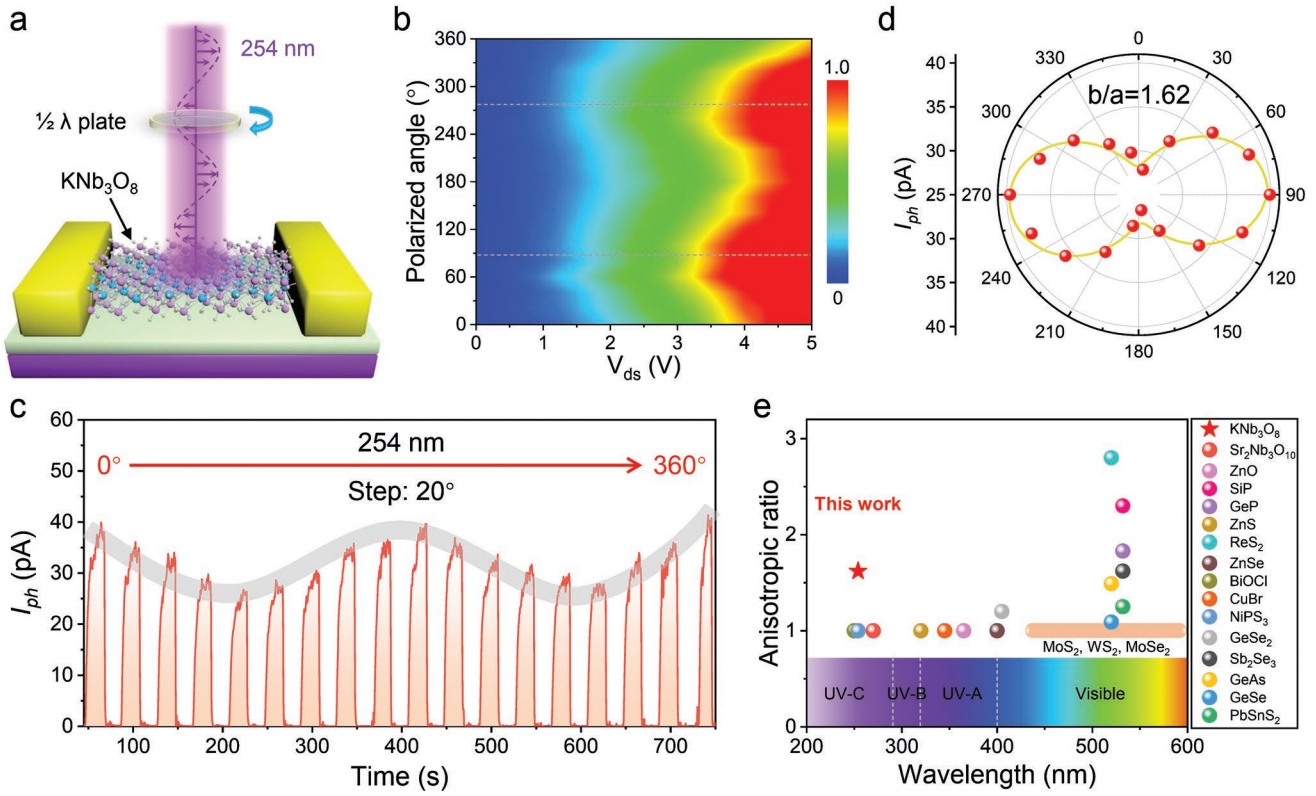

Figure 5. Polarization-sensitive photodetection of ultrathin KNb_3O_8 nanobelts. a) Schematic representation of the polarization-sensitive photodetector based on KNb_3O_8 nanobelt. b) Contour map of polarized photoelectric characteristics of KNb_3O_8 device under 254 nm light irradiation with different polarization angle. c) Time-resolved photoresponse with light polarization direction along 0–180° recorded under 254 nm laser sources. d) Polar plot of the angle-resolved photocurrent under 254 nm linear-polarization laser illumination. e) Comparison of the photocurrent anisotropic ratio and photoresponse range with other common 2D and 1D materials, including $Sr_2Nb_3O_{10}$,[50] ZnO,[51] SiP,[52] GeP,[53] ZnS,[54] ZnSe,[55] ReS_2,[23] BiOCl,[56] CuBr,[21] $NiPS_3$,[57] $GeSe_2$,[20] Sb_2Se_3,[58] GeAs,[24] GeSe,[59] $PbSnS_2$.[60]

(Nb_2O_5) powder (5 mg, Alfa Aelsar, purity 99.9985%) and potassium chloride (KCl) powder (15 mg, Hushi, 99.8%) were used as precursors, the fluorophlogopite mica ($KMg_3AlSi_3O_{10}F_2$) was selected as the growth substrate. At first, a quartz boat containing the mixture of Nb_2O_5 and KCl powder precursors was placed at the center of the tube with a slice mica substrate (1×1 cm^2) faced downward onto the boat. Then, the furnace was heated to 800 °C at a rate of 30 °C min^{-1} with 150 sccm Ar as carrier gas, and maintained at 800 °C for 30 min to grow the samples. After the growth, the furnace was naturally cooled down to room temperature. The as-grown KNb_3O_8 nanobelts were detached from the mica substrate by using a wet-chemical etching technique and then transferred onto the target substrate (copper grid or SiO_2/Si substrate) for further structure and property characterization.

Structure and Composition Characterization: Optical images of KNb_3O_8 samples were obtained by Olympus BX51 optical microscopy. AFM (Bruker Dimension ICON) was used to characterize the surface morphology of KNb_3O_8 nanobelts. XPS (Thermo Fisher Scientific ESCALAB Xi+) and XRD (Smart Lab 9) measurements were carried out to confirm the chemical composition and phase structure of KNb_3O_8 nanobelts. Raman spectra and Raman mapping were acquired on WITec Raman microscope with a 532 nm laser. Angle-resolved polarization Raman spectra were achieved by turning the polarization angle of excitation laser via a half-wave plate. PL spectra were conducted on a confocal micro-Raman spectroscope (Renishaw) with a 375 nm laser. Absorption spectrum was gained from a UV–vis spectrophotometer (Shimadzu UV-3600). TRPL spectrum was performed on an Edinburgh FS5 spectrofluorometer. Atomic structure and element distribution of KNb_3O_8 nanobelts were analyzed via HRTEM and EDX mapping (Titan Cubed Themis G2 300, accelerating voltage, 300 kV).

Device Fabrication and Photoelectrical Measurements: The CVD-grown KNb_3O_8 nanobelts were transferred onto Si/SiO_2 (300 nm) substrate with alignment markers. The metal electrodes (Cr/Au = 5/50 nm) were then patterned on the top of the KNb_3O_8 nanobelts through the standard electron-beam lithography, thermal evaporation deposition and lift-off process in order. The photoelectrical properties of the KNb_3O_8 nanobelt device were measured using a semiconductor characterization system (Keithley 4200, USA) and a four-probe station, and a 450 W Xenon lamp equipped with a monochromator was used as the light source. The power density of the light was measured with a NOVA II power meter (OPHIR Photonics). Polarization-dependent photoresponse was measured by rotating the polarization of the incident light (254 nm laser) using a half-wave plate in the light path. The noise power spectra were measured by a PDA (Platform Design Automation, Inc.). Note that all the electrical and photoelectrical measurements were performed under ambient air condition.

Density Functional Theory Calculations: All calculations were performed using the Vienna Ab Initio Simulation Package (VASP) code, based on density functional theory (DFT). The generalized gradient approximation in the form of Perdrew–Burke–Ernzerhof (PBE) functional was used to describe the electron exchange correlation. The projector augmented wave (PAW) method was applied to describe electron–ion interaction. The cutoff energy for the plane-wave basis was set to be 520 eV and a convergence energy accuracy of 1.0×10^{-5} eV per atom was set for self-consistent field calculation. All the atomic positions and cell parameters were relaxed until the force on each atom was less than 1 meV Å^{-1}. The hybrid DFT based on the Heyd–Scuseria–Ernzerhof (HSE) exchange-correlation functions was adopted to correct the well-known underestimation of the band gap in the PBE calculations.

Supporting Information

Supporting Information is available from the Wiley Online Library or from the author.

Acknowledgements

Y.P., H.L., and H.L. contributed equally to this work. This work was supported by the National Natural Science Foundation of China (Grant Nos. 51972204 and 62125404), the Natural Science Basic Research Plan in Shaanxi Province (Grant No. 2018JQ5192), the Science and Technology Program of Shaanxi Province (Grant No. 2017KJXX-16), and the Fundamental Research Funds for the Central Universities in Shaanxi Normal University (Grant No. GK201802003). Figure 2 and Figure 5 were corrected on June 10, 2022 after initial online publication.

Conflict of Interest

The authors declare no conflict of interest.

Data Availability Statement

Research data are not shared.

Keywords

anisotropy, chemical vapor deposition, KNb_3O_8 nanobelts, solar-blind ultraviolet photodetectors, ultrawide bandgap

Received: November 16, 2021
Revised: December 13, 2021
Published online: January 14, 2022

[1] M. Kneissl, T.-Y. Seong, J. Han, H. Amano, *Nat. Photonics* **2019**, *13*, 233.
[2] Q. Cai, H. F. You, H. Guo, J. Wang, B. Liu, Z. L. Xie, D. J. Chen, H. Lu, Y. D. Zheng, R. Zhang, *Light: Sci. Appl.* **2021**, *10*, 94.
[3] C. Xie, X.-T. Lu, X.-W. Tong, Z.-X. Zhang, F.-X. Liang, L. Liang, L.-B. Luo, Y.-C. Wu, *Adv. Funct. Mater.* **2019**, *29*, 1806006.
[4] M. Razeghi, *Proc. IEEE* **2002**, *90*, 1006.
[5] A. BenMoussa, A. Soltani, K. Haenen, U. Kroth, V. Mortet, H. A. Barkad, D. Bolsee, C. Hermans, M. Richter, J. C. De Jaeger, J. F. Hochedez, *Semicond. Sci. Technol.* **2008**, *23*, 035026.
[6] L. Li, P. S. Lee, C. Y. Yan, T. Y. Zhai, X. S. Fang, M. Y. Liao, Y. Koide, Y. Bando, D. Golberg, *Adv. Mater.* **2010**, *22*, 5145.
[7] J. Li, Z. Y. Fan, R. Dahal, M. L. Nakarmi, J. Y. Lin, H. X. Jiang, *Appl. Phys. Lett.* **2006**, *89*, 213510.
[8] F. P. García de Arquer, A. Armin, P. Meredith, E. H. Sargent, *Nat. Rev. Mater.* **2017**, *2*, 16100.
[9] H. Y. Chen, H. Liu, Z. M. Zhang, K. Hu, X. S. Fang, *Adv. Mater.* **2016**, *28*, 403.
[10] L. Peng, L. F. Hu, X. S. Fang, *Adv. Mater.* **2013**, *25*, 5321.
[11] R. Maiti, C. Patil, M. A. S. R. Saadi, T. Xie, J. G. Azadani, B. Uluutku, R. Amin, A. F. Briggs, M. Miscuglio, D. Van Thourhout, S. D. Solares, T. Low, R. Agarwal, S. R. Bank, V. J. Sorger, *Nat. Photonics* **2020**, *14*, 578.
[12] Y.-Q. Bie, G. Grosso, M. Heuck, M. M. Furchi, Y. Cao, J. Zheng, D. Bunandar, E. Navarro-Moratalla, L. Zhou, D. K. Efetov, T. Taniguchi, K. Watanabe, J. Kong, D. Englund, P. Jarillo-Herrero, *Nat. Nanotechnol.* **2017**, *12*, 1124.
[13] H. Kim, S. Z. Uddin, D.-H. Lien, M. Yeh, N. S. Azar, S. Balendhran, T. Kim, N. Gupta, Y. Rho, C. P. Grigoropoulos, K. B. Crozier, A. Javey, *Nature* **2021**, *596*, 232.
[14] Y. Geng, Y. J. Zhao, J. J. Zhao, Y. Zhai, M. Yuan, X.-D. Wang, H. F. Gao, J. G. Feng, Y. C. Wu, L. Jiang, *SmartMat* **2021**, *2*, 388.
[15] Q. X. Qiu, Z. M. Huang, *Adv. Mater.* **2021**, *33*, 2008126.
[16] Y. Yang, K. X. Zhang, L. B. Zhang, G. Hong, C. Chen, H. M. Jing, J. B. Lu, P. Wang, X. S. Chen, L. Wang, H. Xu, *InfoMat* **2021**, *3*, 705.
[17] F. Wang, Z. X. Wang, L. Yin, R. Q. Cheng, J. J. Wang, Y. Wen, T. A. Shifa, F. M. Wang, Y. Zhang, X. Y. Zhan, J. He, *Chem. Soc. Rev.* **2018**, *47*, 6296.
[18] H. Liu, J. H. Meng, X. W. Zhang, Y. N. Chen, Z. G. Yin, D. G. Wang, Y. Wang, J. B. You, M. L. Gao, P. Jin, *Nanoscale* **2018**, *10*, 5559.
[19] L. X. Kang, X. C. Yu, X. X. Zhao, Q. L. Ouyang, J. Di, M. Z. Xu, D. Tian, W. L. Gan, C. C. I. Ang, S. Ning, Q. D. Fu, J. D. Zhou, R. G. Kutty, Y. Deng, P. Song, Q. S. Zeng, S. J. Pennycook, J. Shen, K.-T. Yong, Z. Liu, *InfoMat* **2020**, *2*, 593.
[20] Y. Yan, W. Xiong, S. Li, K. Zhao, X. Wang, J. Su, X. H. Song, X. P. Li, S. Zhang, H. Yang, X. F. Liu, L. Jiang, T. Y. Zhai, C. X. Xia, J. B. Li, Z. M. Wei, *Adv. Opt. Mater.* **2019**, *7*, 1900622.
[21] C. H. Gong, J. W. Chu, C. J. Yin, C. Y. Yan, X. Z. Hu, S. F. Qian, Y. Hu, K. Hu, J. W. Huang, H. B. Wang, Y. Wang, P. H. Wangyang, T. Y. Lei, L. P. Dai, C. Y. Wu, B. Chen, C. B. Li, M. Liao, T. Y. Zhai, J. Xiong, *Adv. Mater.* **2019**, *31*, 1903580.
[22] C. H. Gong, Y. X. Zhang, W. Chen, J. W. Chu, T. Y. Lei, J. R. Pu, L. P. Dai, C. Y. Wu, Y. H. Cheng, T. Y. Zhai, L. Li, J. Xiong, *Adv. Sci.* **2017**, *4*, 1700231.
[23] X. B. Li, C. Chen, Y. Yang, Z. B. Lei, H. Xu, *Adv. Sci.* **2020**, *7*, 2002320.
[24] Z. Q. Zhou, M. S. Long, L. F. Pan, X. T. Wang, M. Z. Zhong, M. Blei, J. L. Wang, J. Z. Fang, S. Tongay, W. D. Hu, J. B. Li, Z. M. Wei, *ACS Nano* **2018**, *12*, 12416.
[25] E. Z. Zhang, P. Wang, Z. Li, H. F. Wang, C. Y. Song, C. Huang, Z.-G. Chen, L. Yang, K. T. Zhang, S. H. Lu, W. Y. Wang, S. S. Liu, H. H. Fang, X. H. Zhou, H. G. Yan, J. Zou, X. G. Wan, P. Zhou, W. D. Hu, F. X. Xiu, *ACS Nano* **2016**, *10*, 8067.
[26] H. T. Yuan, X. G. Liu, F. Afshinmanesh, W. Li, G. Xu, J. Sun, B. Lian, A. G. Curto, G. J. Ye, Y. Hikita, Z. X. Shen, S.-C. Zhang, X. H. Chen, M. Brongersma, H. Y. Hwang, Y. Cui, *Nat. Nanotechnol.* **2015**, *10*, 707.
[27] X. B. Li, X. Y. Dai, D. Q. Tang, X. Wang, J. H. Hong, C. Chen, Y. Yang, J. B. Lu, J. G. Zhu, Z. B. Lei, K. Suenaga, F. Ding, H. Xu, *Adv. Funct. Mater.* **2021**, *31*, 2102138.
[28] X. Zhou, X. Z. Hu, S. S. Zhou, Q. Zhang, H. Q. Li, T. Y. Zhai, *Adv. Funct. Mater.* **2017**, *27*, 1703858.
[29] F. C. Liu, S. J. Zheng, X. X. He, A. Chaturvedi, J. F. He, W. L. Chow, T. R. Mion, X. L. Wang, J. D. Zhou, Q. D. Fu, H. J. Fan, B. K. Tay, L. Song, R.-H. He, C. Kloc, P. M. Ajayan, Z. Liu, *Adv. Funct. Mater.* **2016**, *26*, 1169.
[30] L. J. Pi, C. G. Hu, W. F. Shen, L. Li, P. Luo, X. Z. Hu, P. Chen, D. Y. Li, Z. X. Li, X. Zhou, T. Y. Zhai, *Adv. Funct. Mater.* **2021**, *31*, 2006774.
[31] W. Yang, J. H. Yang, K. Zhao, Q. Gao, L. Y. Liu, Z. Zhou, S. J. Hou, X. T. Wang, G. Z. Shen, X. C. Pang, Q. Xu, Z. M. Wei, *Adv. Sci.* **2021**, *8*, 2100075.
[32] L. Li, P. L. Gong, D. P. Sheng, S. Wang, W. K. Wang, X. D. Zhu, X. Q. Shi, F. K. Wang, W. Han, S. J. Yang, K. L. Liu, H. Q. Li, T. Y. Zhai, *Adv. Mater.* **2018**, *30*, 1804541.
[33] Y. Yang, S.-C. Liu, X. Wang, Z. B. Li, Y. Zhang, G. M. Zhang, D.-J. Xue, J.-S. Hu, *Adv. Funct. Mater.* **2019**, *29*, 1900411.
[34] J. X. Wu, H. T. Yuan, M. M. Meng, C. Chen, Y. Sun, Z. Y. Chen, W. H. Dang, C. W. Tan, Y. J. Liu, J. B. Yin, Y. B. Zhou, S. Y. Huang, H. Q. Xu, Y. Cui, H. Y. Hwang, Z. F. Liu, Y. L. Chen, B. H. Yan, H. L. Peng, *Nat. Nanotechnol.* **2017**, *12*, 530.

[35] N. H. Miao, B. Xu, L. G. Zhu, J. Zhou, Z. M. Sun, *J. Am. Chem. Soc.* **2018**, *140*, 2417.
[36] C. H. Gong, J. W. Chu, S. F. Qian, C. J. Yin, X. Z. Hu, H. B. Wang, Y. Wang, X. Ding, S. C. Jiang, A. Li, Y. P. Gong, X. F. Wang, C. B. Li, T. Y. Zhai, J. Xiong, *Adv. Mater.* **2020**, *32*, 1908242.
[37] G. Yang, W. Hou, X. Feng, X. Jiang, J. Guo, *Adv. Funct. Mater.* **2007**, *17*, 3521.
[38] K. Nassau, J. W. Shiever, *Appl. Phys. Lett.* **1968**, *12*, 349.
[39] L. H. Li, J. X. Deng, J. Chen, X. Y. Sun, R. B. Yu, G. R. Liu, X. R. Xing, *Chem. Mater.* **2009**, *21*, 1207.
[40] K. McColl, K. J. Griffith, R. L. Dally, R. Li, J. E. Douglas, K. R. Poeppelmeier, F. Corà, I. Levin, M. M. Butala, *J. Mater. Chem. A* **2021**, *9*, 20006.
[41] Y. M. He, X. Q. Dai, S. N. Ma, L. Chen, Z. Feng, P. X. Xing, J. X. Yu, Y. Wu, *Ceram. Int.* **2020**, *46*, 11421.
[42] H. Sun, F. Niu, P. Yuan, X. X. He, J. Sun, Z. H. Liu, Q. Li, Z. B. Lei, *Small Struct.* **2021**, *2*, 2100029.
[43] H. Sun, J. Li, J. Sun, L. Q. Dang, Z. H. Liu, Z. B. Lei, *J. Phys. Chem. C* **2020**, *124*, 11358.
[44] W. W. Meng, X. M. Wang, Z. W. Xiao, J. B. Wang, D. B. Mitzi, Y. F. Yan, *J. Phys. Chem. Lett.* **2017**, *8*, 2999.
[45] R. Li, L. Y. Liu, B. M. Ming, Y. H. Ji, R. Z. Wang, *Appl. Surf. Sci.* **2018**, *439*, 983.
[46] O. Lopez-Sanchez, D. Lembke, M. Kayci, A. Radenovic, A. Kis, *Nat. Nanotechnol.* **2013**, *8*, 497.
[47] E. F. Liu, M. S. Long, J. W. Zeng, W. Luo, Y. J. Wang, Y. M. Pan, W. Zhou, B. G. Wang, W. D. Hu, Z. H. Ni, Y. M. You, X. A. Zhang, S. Q. Qin, Y. Shi, K. Watanabe, T. Taniguchi, H. T. Yuan, H. Y. Hwang, Y. Cui, F. Miao, D. Y. Xing, *Adv. Funct. Mater.* **2016**, *26*, 1938.
[48] D. Kim, K. Park, J. H. Lee, I. S. Kwon, I. H. Kwak, J. Park, *Small* **2021**, *17*, 2006310.
[49] Y. Yan, J. H. Yang, J. Du, X. M. Zhang, Y.-Y. Liu, C. X. Xia, Z. M. Wei, *Adv. Mater.* **2021**, *33*, 2008761.
[50] S. Y. Li, Y. Zhang, W. Yang, H. Liu, X. S. Fang, *Adv. Mater.* **2020**, *32*, 1905443.
[51] Y. Zhang, X. y. Zhao, J. X. Chen, S. Y. Li, W. Yang, X. S. Fang, *Adv. Funct. Mater.* **2020**, *30*, 1907650.
[52] S. Q. Zhao, P. Luo, S. J. Yang, X. Zhou, Z. Z. Wang, C. L. Li, S. P. Wang, T. Y. Zhai, X. T. Tao, *Adv. Opt. Mater.* **2021**, *9*, 2100198.
[53] L. Li, W. K. Wang, P. L. Gong, X. D. Zhu, B. Deng, X. Q. Shi, G. Y. Gao, H. Q. Li, T. Y. Zhai, *Adv. Mater.* **2018**, *30*, 1706771.
[54] X. S. Fang, Y. Bando, M. Y. Liao, U. K. Gautam, C. Y. Zhi, B. Dierre, B. Liu, T. Y. Zhai, T. Sekiguchi, Y. Koide, D. Golberg, *Adv. Mater.* **2009**, *21*, 2034.
[55] X. S. Fang, S. L. Xiong, T. Y. Zhai, Y. Bando, M. Y. Liao, U. K. Gautam, Y. Koide, X. G. Zhang, Y. T. Qian, D. Golberg, *Adv. Mater.* **2009**, *21*, 5016.
[56] W. Han, C. Li, S. J. Yang, P. Luo, F. K. Wang, X. Feng, K. L. Liu, K. Pei, Y. Li, H. Q. Li, L. Y. Li, Y. H. Gao, T. Y. Zhai, *Small* **2020**, *16*, 2000228.
[57] J. W. Chu, F. M. Wang, L. Yin, L. Lei, C. Y. Yan, F. Wang, Y. Wen, Z. X. Wang, C. Jiang, L. P. Feng, J. Xiong, Y. R. Li, J. He, *Adv. Funct. Mater.* **2017**, *27*, 1701342.
[58] Z. P. Ma, S. N. Chai, Q. L. Feng, L. Li, X. B. Li, L. Huang, D. Y. Liu, J. Sun, R. B. Jiang, T. Y. Zhai, H. Xu, *Small* **2019**, *15*, 1805307.
[59] X. T. Wang, Y. T. Li, L. Huang, X.-W. Jiang, L. Jiang, H. L. Dong, Z. M. Wei, J. B. Li, W. P. Hu, *J. Am. Chem. Soc.* **2017**, *139*, 14976.
[60] Z. W. Shu, Q. J. Peng, P. Huang, Z. Xu, A. A. Suleiman, X. W. Zhang, X. D. Bai, X. Zhou, T. Y. Zhai, *Matter* **2020**, *2*, 977.
[61] M. Hafeez, L. Gan, H. Q. Li, Y. Ma, T. Y. Zhai, *Adv. Mater.* **2016**, *28*, 8296.
[62] F. F. Cui, X. Li, Q. L. Feng, J. B. Yin, L. Zhou, D. Y. Liu, K. Q. Liu, X. X. He, X. Liang, S. Z. Liu, Z. B. Lei, Z. H. Liu, H. L. Peng, J. Zhang, J. Kong, H. Xu, *Nano Res.* **2017**, *10*, 2732.
[63] C. K. Wang, S. J. Chang, Y. K. Su, Y. Z. Chiou, C. S. Chang, T. K. Lin, H. L. Liu, J. J. Tang, *Semicond. Sci. Technol.* **2005**, *20*, 485.
[64] S. M. Hatch, J. Briscoe, S. Dunn, *Adv. Mater.* **2013**, *25*, 867.